SHORT COMMUNICATION

Application of the lattice Boltzmann method to flow in aneurysm with ring-shaped stent obstacles

X. Xu and J. S. Lee*,†

Department of Mechanical Engineering, Wayne State University, 5050 Anthony Wayne Dr. No. 2100, Detroit, MI 48202, U.S.A.

SUMMARY

To resolve the characteristics of a highly complex flow, a lattice Boltzmann method with an extrapolation boundary technique was used in aneurysms with and without transverse objects on the upper wall, and results were compared with the non-stented aneurysm. The extrapolation boundary concept allows the use of Cartesian grids even when the boundaries do not conform to Cartesian coordinates. To ease the code development and facilitate the incorporation of new physics, a new scientific programming strategy based on object-oriented concepts was developed. The reduced flow, smaller vorticity magnitude and wall shear stress, and smaller du/dy near the dome of the aneurysm were observed when the proposed stent obstacles were used. The height of the stent obstacles was more effective to reduce the vorticity near the dome of the aneurysm than the width of the stent. The rectangular stent with 20% height-of-vessel radius was observed to be optimal and decreased the magnitude of the vorticity by 21% near the dome of the aneurysm. Copyright © 2008 John Wiley & Sons, Ltd.

INTRODUCTION

Studies of aneurysm models have shown complex hemodynamic changes in an aneurysm after the placement of a stent across the aneurysm neck [1–5]. But an irregularly shaped and wide-necked aneurysm makes the current stent technology limited [6]. Doctors, sometimes, use lack of

---

*Correspondence to: J. S. Lee, Department of Mechanical Engineering, Wayne State University, 5050 Anthony Wayne Dr. No. 2100, Detroit, MI 48202, U.S.A.
†E-mail: joonlee@wayne.edu

a variety of sizes of stents for the artery being treated due to the short supply of stents. This can cause serious results such as subacute thrombosis [7]. Any alternative surgical supplies that can be manufactured easily and flexibly performed with complex vessel geometry should provide more options and prevent doctors from using stents that are poorly matched to the size of the vessel.

The flow over two- and/or three-dimensional obstacles of different shapes and sizes has been studied extensively by numerous investigators due to its importance to engineering applications. In many of these applications, enhanced surfaces significantly alter the structure of the flow. Han *et al.* [8] conducted an experimental study to investigate the effect of rib geometry on the friction factor for complex flow. It was found that the shape and size of the rib affected the friction factor significantly.

Bergeles and Athanassiadis [9] studied the influence of the streamwise length of a rib on reattachment length and showed that a sudden decrease in reattachment length from 11 to 3 rib heights was observed when the length-to-height ratio of a rib was greater than 4. Sparrow and Tao [10] used the naphthalene sublimation technique in flat rectangular channels of large aspect ratios with obstacles situated on one of the walls of the channel and oriented transversely to the flow direction. The results showed a substantial enhancement of the Sherwood (Sh) number compared with the smooth-wall duct. Drain and Martin [11] performed laser Doppler velocimetry measurements of the fully developed water flow in a rectangular duct with one surface roughened with a periodic array of elements. They found that the conventional Navier–Stokes (NS) equation solver tended to seriously underestimate the reattachment length, which is an importance indicator of complex flow structure.

In this paper a lattice Boltzmann method (LBM) was considered for the simulation of an aneurysm. One advantage of the LBM is that data communications between nodes are always local, which makes the method extremely efficient for large-scale parallel computations [12]. It is also easy to handle complex geometry including moving boundaries without the loss of computational speed. The LBM has been applied to many engineering and science problems including turbulence [13], porous media flow [14], multiphase flows [15] and physiological flows [16, 17]. Figure 1 shows flow regimes in terms of the Knudsen (Kn) number and indicates how widely the LBM can be used. The NS and Euler equations are applicable when $Kn<0.01$ (continuum) or <0.1 when appropriate slip boundary treatments are used. With the Boltzmann equation, most of the flow regimes are covered ($Kn<100$).

The goal of this study was to perform a two-dimensional planar lattice Boltzmann simulation of flows in aneurysms with and without a transverse stent obstacle on the upper wall to analyze the flow mechanics inside the artery, paying close attention to the effects of the disease geometry with a proposed complex boundary treatment method. Throughout this study, the simple two-dimensional
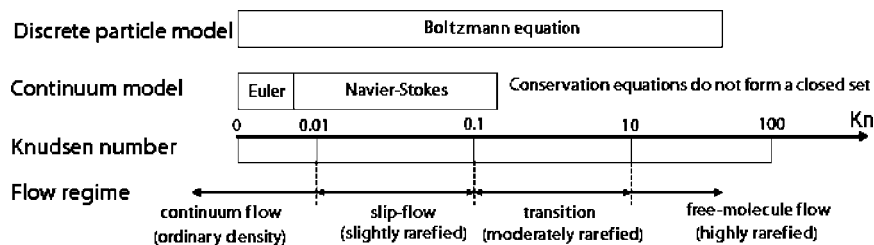

Figure 1. Knudsen numbers and corresponding governing equations [18].

geometry for the aneurysm was considered. The pulsatile boundary condition was used at the inflow boundary. To avoid a large computational demand, the ghost cell extrapolation method was used in this study.

NUMERICAL METHOD AND CODE DEVELOPMENT STRATEGY

The LBM

The LBM used in this study is the nine-velocity incompressible lattice Bhatnagar–Gross–Krook (BGK) model (D2Q9) [19–21] as shown in Figure 2. The evolution of the distribution function $f_i(x, t)$ on a lattice is governed by

$$\frac{\partial f}{\partial t} + \mathbf{e} \cdot \nabla f = \Omega(f) \tag{1}$$

with the conservation of mass, momentum and Galilean invariance. The fluid density, ρ, and velocity, $\mathbf{u}$, can be evaluated from the distribution function by

$$\rho = \int f(\mathbf{x}, \mathbf{e}, t) \, dV, \quad \rho\mathbf{u} = \int \mathbf{e} f(\mathbf{x}, \mathbf{e}, t) \, dV \tag{2}$$

In the D2Q9 BGK model, the evolution of the distribution function on a lattice (Equation (1)) is discretized as follows:

$$\frac{\partial f_i}{\partial t} + \mathbf{e}_i \cdot \nabla f_i = \Omega_i(f) \quad (i = 0, 1, 2, \ldots, 8) \tag{3}$$

The distribution functions contribute to the density, ρ, and the fluid momentum, $\rho\mathbf{u}$ obtained from Equation (2) by the following equations:

$$\rho = \sum_{i=0}^{8} f_i(\mathbf{x}, \mathbf{e}, t), \quad \rho\mathbf{u} = \sum_{i=0}^{8} \mathbf{e}_i f_i(\mathbf{x}, \mathbf{e}, t) \tag{4}$$

The directions of discrete velocity used in the model are given by

$$e_i = \begin{cases} (0,0), & i = 0 \\ c(\cos(i-1)\pi/2, \sin(i-1)\pi/2), & i = 1, 2, 3, 4 \\ \sqrt{2}c(\cos(2i-9)\pi/2, \sin(2i-9)\pi/2), & i = 5, 6, 7, 8 \end{cases} \tag{5}$$

where $c = \Delta x / \Delta t$ is the particle speed, and Δx and Δt are the lattice spacing and the time step, respectively.

The evolution of the particle distribution function resulting from the collision processes and the particle propagation is governed by

$$f_i(\mathbf{x} + e_i \Delta t, t + \Delta t) - f_i(\mathbf{x}, t) = -\frac{1}{\tau}(f_i(\mathbf{x}, t) - f_i^{eq}(\mathbf{x}, t)) \quad (i = 0, 1, \ldots, 8) \tag{6}$$

where $(1/\tau)(f_i(\mathbf{x}, t) - f_i^{eq}(\mathbf{x}, t))$ is the collision operator (Ω_i) and τ is the relaxation time. The equilibrium form of the distribution function in two dimensions for the D2Q9 lattice is given by

$$f_i^{eq} = \rho\varpi_i \left[1 + \frac{1}{c_s^2} \mathbf{e}_i \cdot \mathbf{u} + \frac{1}{2c_s^4} (\mathbf{e}_i \cdot \mathbf{u})^2 - \frac{1}{2c_s^2} \mathbf{u} \cdot \mathbf{u} \right] \tag{7}$$
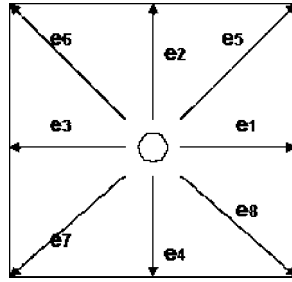
Figure 2. The D2Q9 lattice. The node is the blank circle and fictitious particle
velocities (e_i) have eight directions.

where $c_s(=c/\sqrt{3})$ is the speed of sound, $\omega_0=4/9, \omega_i=1/9$ for $i=1,2,3,4$ and $\omega_i=\frac{1}{36}$ for $i=5,6,7,8$.

The relaxation time, τ, is related to the kinematic viscosity, v, by

$$v=(\tau-\tfrac{1}{2})c_s^2\Delta t \tag{8}$$

Boundary conditions

To validate the LBM, four types of boundary conditions, which include bounce-back, periodic, extrapolation method and extrapolated outlet boundary condition, were used. Each method is briefly described as follows:

Bounce-back boundary condition. The bounce-back boundary condition is the most common and simplest. But this method is only the first order in terms of numerical accuracy [22] unless the boundary is at the center between lattice nodes. It is also not feasible to be applied to such complex boundary conditions as moving boundaries or complex geometries. Therefore, some other boundary treatments have been proposed to improve it. Skordos [23] proposed to include velocity gradients in the equilibrium distribution function at the wall nodes. He and Zou [24] extended the bounce-back condition for the non-equilibrium portion of the distribution. Inamouro *et al.* [25] proposed a non-slip boundary condition by assuming the unknown distributions at the wall to be an equilibrium distribution with a counter slip velocity, which cancels a slip velocity at the wall. However, it is still difficult to implement all the above bounce-back schemes to arbitrary geometries.

In this study, the bounce-back method was applied in a way that a fluid particle colliding with a boundary site simply reverses the direction of its velocity. Figure 3 shows nodal distributions for a simple case. The bounce-back scheme at node B can be expressed as

$$f_2(B)=\tilde{f}_4(F), \quad f_5(B)=\tilde{f}_7(G), \quad f_6(B)=\tilde{f}_8(E) \tag{9}$$

where $\tilde{f}$ is the distribution function after the collision process.

Periodic boundary conditions. For the inlet and outlet, periodic boundaries in combination with velocity and pressure boundaries have been used [26–29]. This will provide simple treatments for inlet and outlet boundaries, but realistic flow conditions (e.g. pulsatile flow) cannot be implemented. Using Figure 1, the periodic condition was applied to the inlet nodes as it was simply transposed
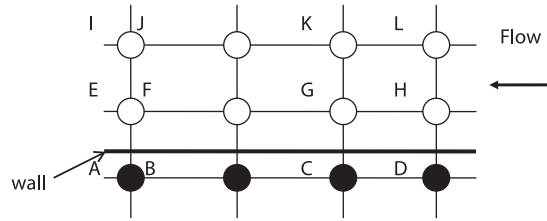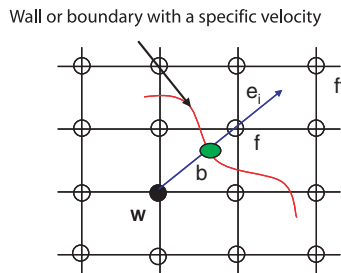
Figure 3. Nodal distributions.

Figure 4. Complex inflow and wall boundary treatments using an extrapolation method.

copies of the outlet nodes at the matching periodic boundary. The relationship between the inlet and outlet nodes is given by

$$f_3(H) = \tilde{f}_3(F), \quad f_3(L) = \tilde{f}_3(I) \tag{10}$$

Extrapolation method. Most of the earlier variations of the immersed boundary method solved the governing equation both inside and outside of the actual flow boundary but used a forcing function to meet the conditions on the boundary. However, it is not practical to solve the fluid equations inside a solid body due to large CPU time consumption [30, 31]. To avoid this, the ghost cell extrapolation method was used for this study based on Guo and Zheng [32]. Figure 4 shows an arbitrary geometry and surrounding nodes. Here nodes, w, b, f and ff, denote the nodes inside the wall, on the boundary, on the fluid adjacent to the wall boundary, and on the fluid next to the fluid lattice, respectively. The distribution function at the wall node, $f_i(\mathbf{x}_w)$, is expressed using a simple relationship:

$$f_i(\mathbf{x}_w) = f_i^{\text{eq}}(\mathbf{x}_w) + f_i^{\text{ne}}(\mathbf{x}_w) \tag{11}$$

where superscripts, eq and ne, denote the equilibrium and non-equilibrium components of the distribution functions, respectively. The equilibrium distribution function, $f_i^{\text{eq}}(\mathbf{x}_w)$, is given by

$$f_i^{\text{eq}}(\mathbf{x}_w) = \rho_w \omega_i \left[1 + \frac{1}{c_s^2} \mathbf{e_i} \cdot \mathbf{u}_w + \frac{1}{2c_s^4} (\mathbf{e}_i \cdot \mathbf{u}_w)^2 - \frac{1}{2c_s^2} \mathbf{u}_w \cdot \mathbf{u}_w \right] \tag{12}$$

where $\mathbf{u}_w$ is extrapolated by

$$\mathbf{u}_w = \mathbf{u}_{w1}, \quad \Delta \geqslant 0.75$$
$$\mathbf{u}_w = \Delta \mathbf{u}_{w1} + (1-\Delta)\mathbf{u}_{w2}, \quad \Delta < 0.75 \tag{13}$$

where Δ, $\mathbf{u}_{w1}$ and $\mathbf{u}_{w2}$ are defined as

$$\Delta = \frac{|\mathbf{x}_f - \mathbf{x}_b|}{|\mathbf{x}_f - \mathbf{x}_w|}, \quad \mathbf{u}_{w1} = (\mathbf{u}_b + (\Delta - 1)\mathbf{u}_f)/\Delta, \quad \mathbf{u}_{w2} = (2\mathbf{u}_b + (\Delta - 1)\mathbf{u}_{ff})/(1+\Delta) \quad (14)$$

Finally, the non-equilibrium part of the wall distribution function, $f_i^{ne}(\mathbf{x}_w)$, is

$$f_i^{ne}(\mathbf{x}_w) = \Delta f_i^{ne}(\mathbf{x}_f) + (1-\Delta)f_i^{ne}(\mathbf{x}_{ff}) \quad (15)$$

The extrapolation scheme is of the second-order accuracy, and it is consistent with the accuracy of the D2Q9 model [32]. This scheme is also expected to yield more accurate results compared with the bounce-back scheme [32].

Linear extrapolation outlet boundary condition. The unknown distribution functions are extrapolated at the outlet boundary using the inner lattice right before the outlet boundary at the streaming time step [33]. Only three distribution functions, f_3, f_6 and f_7 are extrapolated

$$f(\mathbf{x}, t+\Delta t) = 2f_i(\mathbf{x}+e_i\Delta t, t+\Delta t) - f_i(\mathbf{x}+2e_i\Delta t, t+\Delta t) \quad (i=3,6,7) \quad (16)$$

Code development strategy

In this study, the diameter of the artery is larger than 1 mm, and the blood is assumed to be a Newtonian fluid, and a single phase flow simulation is conducted. In the object-oriented program (OOP), software objects are data groupings tightly coupled to procedures for operating on that data. OOP commonly employs objects with the attributes of real-world entities. For example, the LBM fluid solver includes 'Fluid,' 'Field' and 'Grid' objects; most function operations, such as stream and relaxation operations, are conducted in the 'Field' class. By using the OOP strategy, the code was cleaner and easier to manipulate, and it helped to ease the code development and
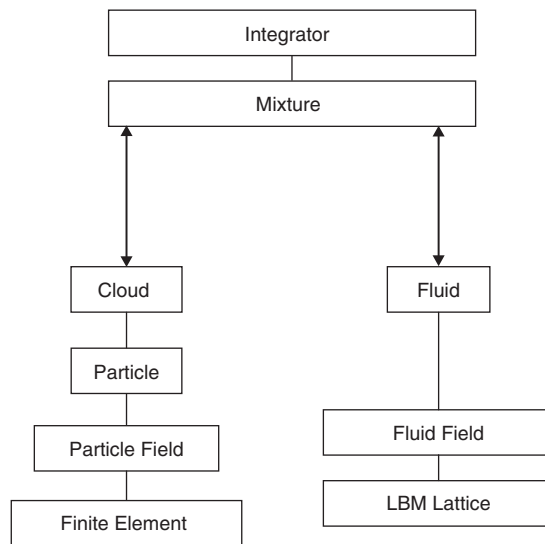

Figure 5. The structure of object-oriented code structures for multi-physics flow.

facilitate the incorporation of new physics. The author has recently published two articles [34, 35] in *Scientific Programming*, detailing the implementation of OOP strategy in scientific software engineering and demonstrating the benefits for code maintainability and reusability while using the OOP strategy. Figure 5 shows the multi-physics code structure.

RESULTS

Validation

Simulation capability to a variety of configurations with respect to the type of flow conditions to obtain a comprehensive comparison with analytical data was conducted. This validated the accuracy of the numerical approach. The fully developed channel flow driven by a constant pressure
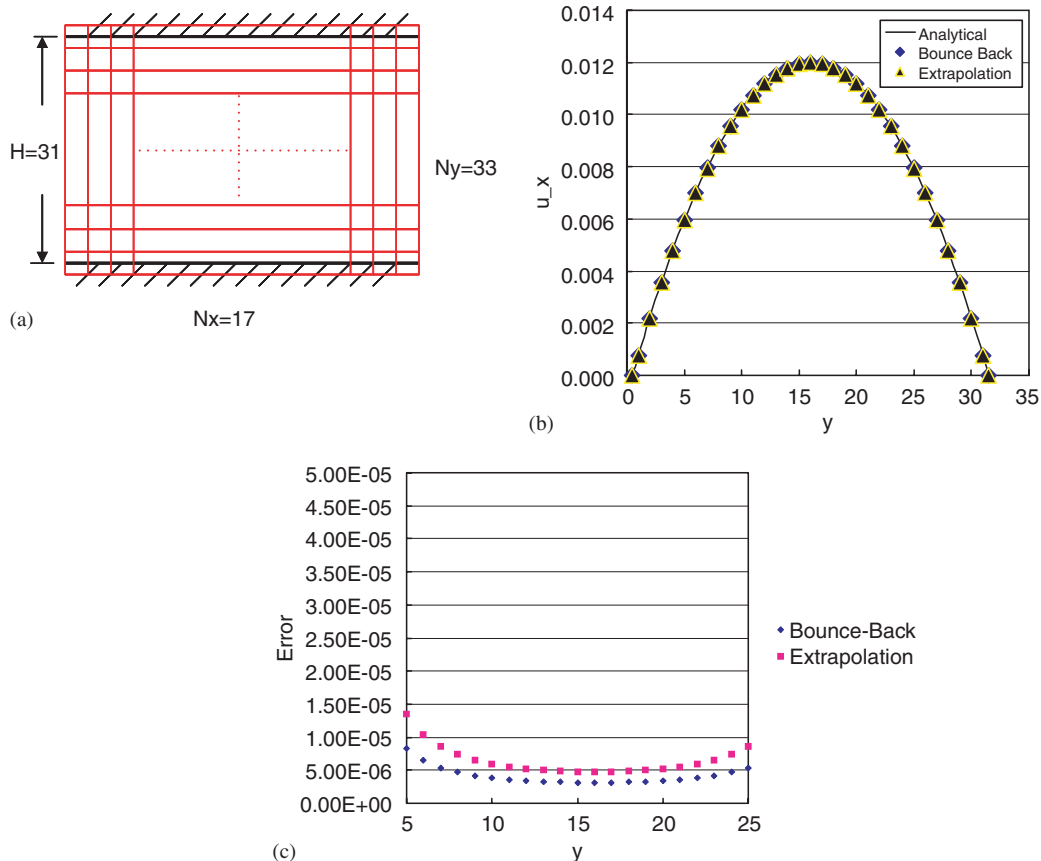
Figure 6. The comparison of fully developed channel flow cases. Analytical, bounce-back and extrapolation schemes are tested and verified: (a) computational domain of the fully developed channel; (b) velocity comparisons with the analytical solution; and (c) the relative error comparisons.

gradient is shown in Figure 6(a). Periodic boundary condition is used at the inlet and outlet, both bounce-back and extrapolation wall boundary conditions are applied on the wall, respectively, for comparison purposes. The profile of the analytical velocity (u_{exact}) [36] is expressed as parabolic

$$u_{exact} = -\frac{1}{2}\frac{dp}{dx}\frac{H^2}{\rho v}\left[\left(\frac{y}{H}\right)^2 - \left(\frac{y}{H}\right)\right] \tag{17}$$

where the non-dimensional values of pressure gradient, $dp/dx = 3 \times 10^{-6}$, kinematic viscosity, $v = 0.03$, density, $\rho = 1$, and H is the channel height, respectively. The Reynolds number of the flow is defined by $Re = u_{max}H/\rho v = 0.012 \times 31/0.03 = 12.4$. The maximum Mach number ($M_{max} = u_{max}/c_s$) is fixed to be 0.021. For the boundary wall treatment, both second-order bounce-back and extrapolation schemes were used and compared as shown in Figure 6(b). The profiles of velocity show that the lattice Boltzmann solutions match the analytical solutions within a few percent. A higher order of accuracy was studied by measuring the convergence rate of the relative error as shown in Figure 6(c). The relative error is defined as

$$Error = \frac{\sqrt{(u - u_e)^2}}{u_e} \tag{18}$$

where u is the numerical solution and u_e is the analytical solution. A very low relative error was generated with both bounce-back and extrapolation methods as shown in Figure 6(c). The error increases with movement toward the stationary wall since u_e is close to zero. A relatively smaller error with the bounce-back method compared with the extrapolation method is observed. However, as the degree of complexity of the geometry increases, the bounce-back method may not work well [37].

The second validation of the LBM is presented in Figure 7. For this, the efficiency of the extrapolation scheme in a Couette flow with a rotating inner wall was investigated. The computational domain for the Couette flow is shown in Figure 7(a), and Cartesian grid points around circular boundaries are shown in Figure 7(b). Extrapolation wall boundary is applied on the wall to accurately capture the circular boundaries. An 80×80 computational domain in the x- and y-directions was employed where the speed of the inner wall (u_0) was fixed to be 0.04. The Reynolds number based on an inner and outer wall radius difference was 53 ($Re = u_0(r_2 - r_1)/v$). In a steady-state
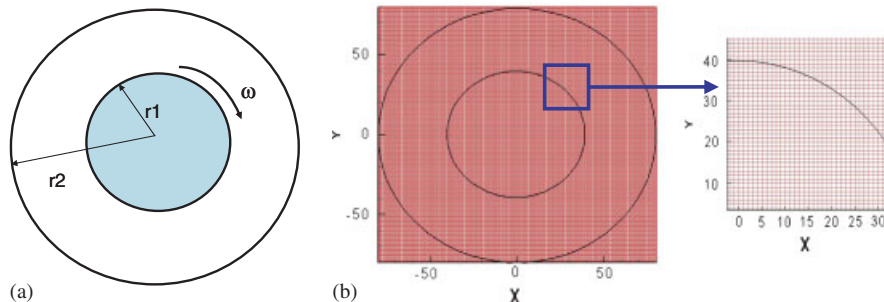

Figure 7. The Couette flow geometry and corresponding grid: (a) the Couette flow configuration and (b) grid generation around the circular.

case, the Couette flow has the following analytical solution [36]:

$$u_\theta(r) = \frac{u_0\beta}{1-\beta^2}\left(\frac{r_2}{r} - \frac{r}{r_2}\right) \tag{19}$$

where $\beta = r_1/r_2$. A good match with the analytical solution is observed in Figure 8(a). Figure 8(b) shows the corresponding velocity vector plot. The relative error (Equation (18)) plot in Figure 8(c) also shows very small error between the numerical and analytical solutions.

Before further study the influence of a transverse stent obstacle on the flow inside the aneurysm, current LB method has been extensively validated by simulating the flow inside an aneurysm using the model SSa LS in [26]. The current simulation used periodic boundary condition at the inlet and outlet as in [26], grid resolutions, 800×188, viscosity, 0.026, and pressure gradient, $4.17e-6$ were used to exactly simulate the referred case in [26]. The only difference between the current simulation and that in [26] is the wall boundary treatment; the bounce-back wall boundary condition was used by Hirabayashi *et al*. [26], whereas the second-order extrapolation method
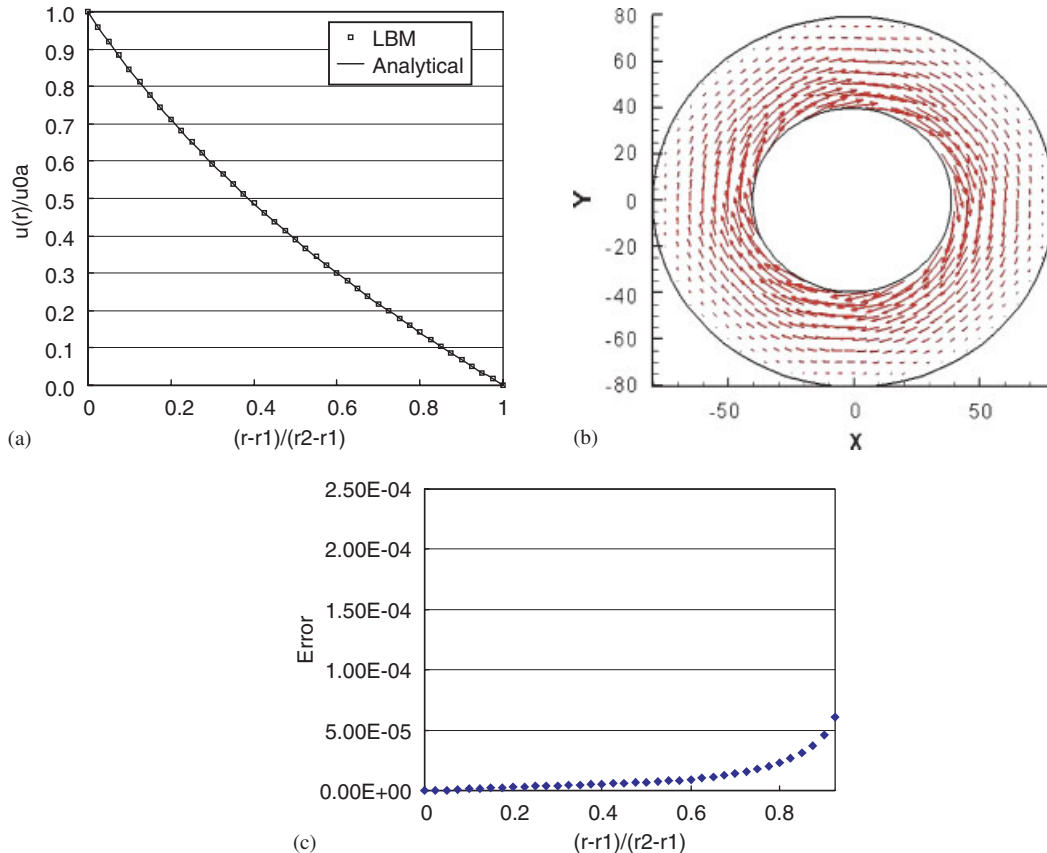

Figure 8. The Couette flow case results: (a) comparison with the analytical solution; (b) velocity vector plot; and (c) the relative error plot.
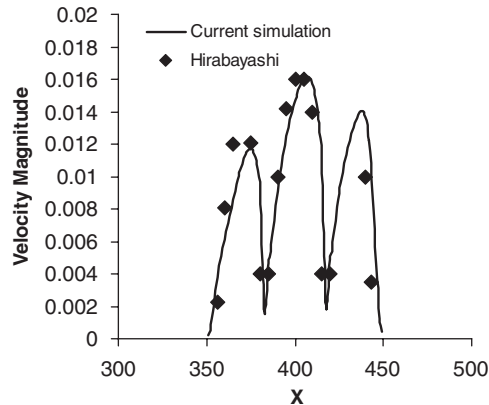
Figure 9. Velocity magnitude comparison at the aneurysm orifice.

was used in the current simulation. The velocity magnitude comparison at the aneurysm orifice in Figure 9 shows that current results matched well with the data of Hirabayashi *et al.* [26].

Flows in aneurysm with a transverse stent obstacle

Despite its capability of reducing blood flows into an aneurysm sac, there are still some problems when the stented aneurysm is used. Won *et al.* [38] investigated problems encountered during and after stent–graft treatment including stent–graft migration, stent–graft folding, cerebral ischemia and mechanical failure. The porosity and size of the stent and the difficulty in implementation to complex vessel geometry are notable problems. The modification of the flow field also causes coagulation in the aneurysm leading to its permanent occlusion after treatment [39]. Therefore, minimal flow changes by the disease treatment and the ease of implementation to the patient-specific geometry are very important. In this section, a simple ring-shaped obstacle situated before an aneurysm was used to examine the effect of the flow in an aneurysm.

The two-dimensional computational domain is shown in Figure 10. The parent vessel is 4 mm in diameter, and the diameter of the sac of the aneurysm is 5 mm. Because the vessel diameter is larger than 1 mm (i.e. it falls in the region of high strain rates), the non-Newtonian effect is small, and the flow is assumed to be Newtonian fluid with the dynamic viscosity of $3.5 \times 10^{-6}\,\text{m}^2/\text{s}$ and the density of $1060\,\text{kg/m}^3$. For simplicity, the vessel wall is treated as rigid. At the entry of the artery, the pulsatile inlet velocity as shown in Figure 11 was implemented by using the extrapolation method to investigate the effects of momentum variations with the different sizes and shapes of the obstacle. The unknown distribution function at the exit is obtained from the extrapolation method. The maximum Reynolds number calculated at $t = 0.3\,\text{s}$, where the maximum center velocity is 0.29 m/s, is

$$Re_{\max} = \frac{u_{\max}\,d}{v} = \frac{0.29\,\text{m/s} \times 0.004\,\text{m}}{3.5 \times 10^{-6}\,\text{m}^2/\text{s}} \approx 331 \tag{20}$$

A ring-shaped stent obstacle can be easily inserted as shown in Figure 12. The ring was positioned in a way that the stent obstacle was directly opposed normal to the main flow direction as shown in Figure 12. A memory-shaped material can be used so that the ring shape will be
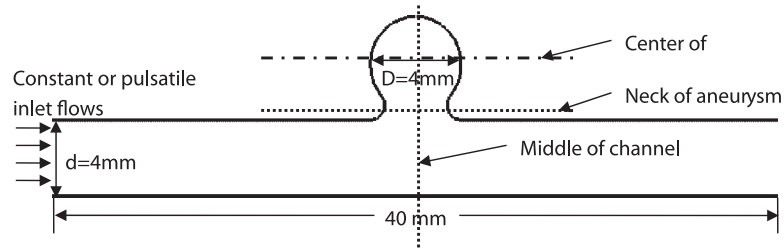
Figure 10. Two-dimensional computational domain of the aneurysm model.
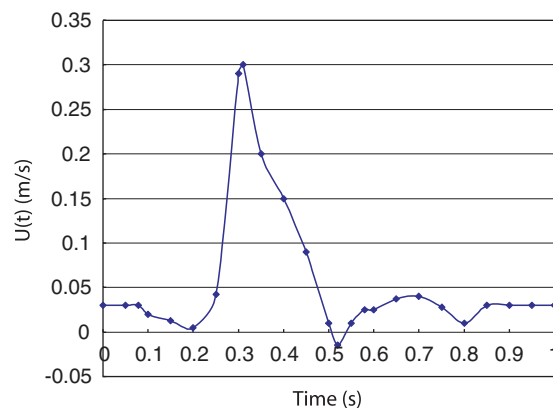
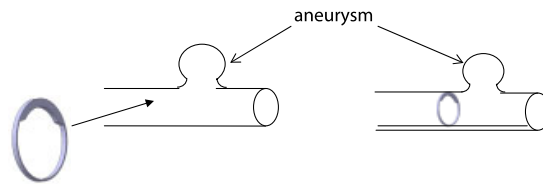

Figure 11. Pulsatile inlet velocity profile.

Figure 12. Ring-shaped stent obstacle is inserted to the desired location.

recovered at the temperature close to that of human blood. This method, however, needs to be tested further in a clinical setting. The geometry for the obstacle is depicted in Figure 13. The ratio of obstacle height (H) to vessel diameter (d) and obstacle length (L) to vessel diameter (d) are given in Table I. Calculations were performed for various cases with triangle-, square- and bluff-shaped stents. Since aneurysm rupture usually occurs at the apex of the dome [40], the analysis of flow effects due to the obstacle was focused on the location of an aneurysm near the dome of the aneurysm.
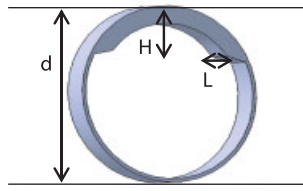
Figure 13. The geometric configuration of a stent obstacle.

Table I. List of studied obstacle cases.

Case	Stent	H/d	L/d
No stent	N/A	N/A	N/A
Triangular stent ($0.1dH\_0.1dL$)		0.1	0.1
Rectangular stent ($0.1dH\_0.1dL$)		0.1	0.1
Rectangular stent ($0.1dH\_0.3dL$)		0.1	0.3
Half circular stent ($0.1dH\_0.2dL$)		0.1	0.2
Half circular stent ($0.1dH\_0.4dL$)		0.1	0.4
Triangular stent ($0.2dH\_0.1dL$)		0.2	0.1
Rectangular stent ($0.2dH\_0.1dL$)		0.2	0.1
Rectangular stent ($0.2dH\_0.3dL$)		0.2	0.3
Half circular stent ($0.2dH\_0.4dL$)		0.2	0.4
Half circular stent ($0.2dH\_0.6dL$)		0.2	0.6

The variables used in this section were non-dimensionalized with respect to a reference velocity, c, density, ρ_0^*, and time step, Δt^* as follows:

$$u=\frac{u^*}{c^*}, \quad v=\frac{v^*}{c^*}, \quad \rho=\frac{\rho^*}{\rho_0^*}, \quad p=\frac{p^*}{\rho_0^* c^{*2}}, \quad \gamma=\frac{\gamma^*}{c^{*2}\Delta t^*} \tag{21}$$

where $c^*=\Delta x^*/\Delta t^*=10^{-4}\,\mathrm{m}/10^{-6}\,\mathrm{s}=100\,\mathrm{m/s}$, $\rho_0^*=1060\,\mathrm{kg/m^3}$.

Figure 14 shows the results of a grid independence study using the non-stented aneurysm model. In this study, the periodic boundary condition is implemented at the inlet and outlet by using the
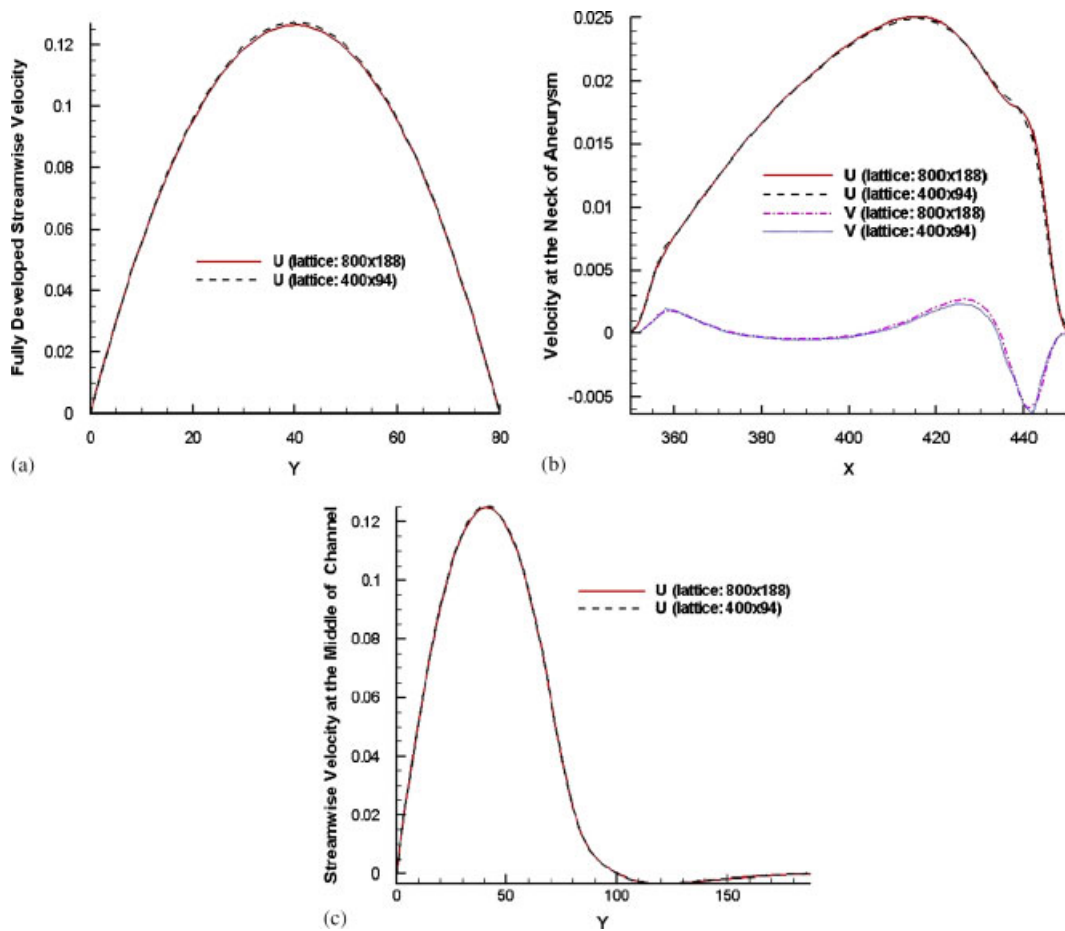
Figure 14. A grid-independent study: (a) fully developed streamwise velocity; (b) velocity at the neck of the aneurysm; and (c) streamwise velocity at the middle of the channel.

constant pressure gradient $dp/dx = 4.17 \times 10^{-6}$. The grid resolution of 400×94 and 800×188 were used with 40 lattices and 80 lattices for the diameter of the vessel, respectively. The results showed good agreement between the grid resolution 400×94 and 800×188; therefore, the grid resolution 400×94 was used in the rest of simulations. The reason for not using coarser grid resolution is because the stent geometry is too small ($1\,\text{mm} \times 1\,\text{mm}$) to be accurately captured by coarser lattices, such as 200×47 ($dx = 2\,\text{mm}$).

Extrapolation wall boundary condition was applied on the wall for the boundary of the aneurysm. Inlet was also treated using the extrapolation wall boundary method by imposing time-dependent pulsatile velocity values. The extrapolation outlet boundary method was used at the outlet. One million time steps were used in one pulsatile period and the time step, Δt, was $10^{-6}\,\text{s}$.

The vorticity contours of the non-stented case during one pulsatile period of the flow near the dome of an aneurysm are shown in Figure 15. It was observed that the highest vorticity corresponds to the time of the peak velocity at $t = 0.3T$ where $T = 1.0\,\text{s}$. Therefore, the data analysis was mostly
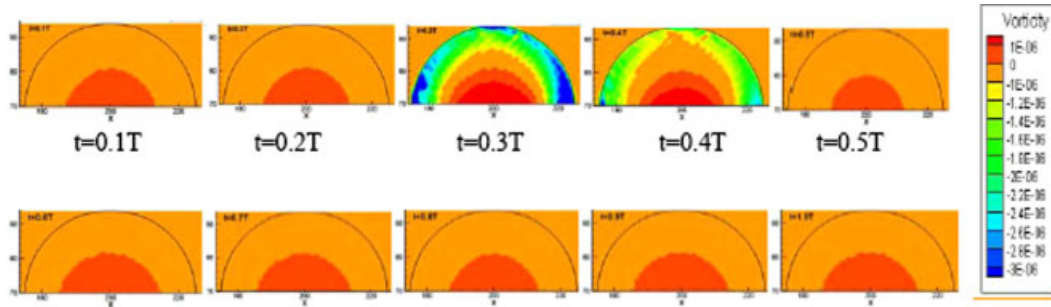
Figure 15. Vorticity contour in one pulsatile cycle for a non-stented aneurysm case.
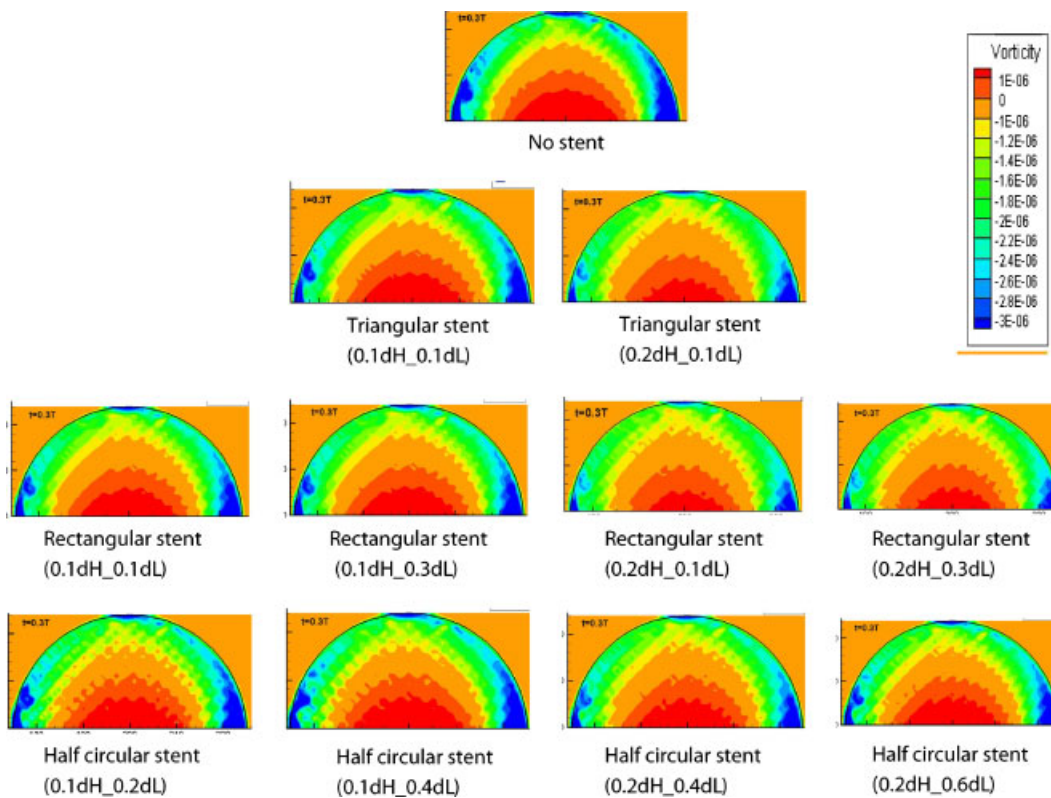
Figure 16. Comparison of vorticity contour at $t = 0.3T$.

conducted at $t = 0.3T$ (i.e. when the highest vorticity appears near the dome area of the aneurysm) in this study.

Figure 16 shows the comparison of vorticity contours between non-stented and different stent (obstacle) shape cases at $t = 0.3T$. It shows that the rectangular stents with $H/d = 0.2$ resulted in the largest vorticity reduction, 21%, compared with the non-stented aneurysm at the dome of

Figure 17. Comparison of $\mathrm{d}u/\mathrm{d}y$ contour at $t=0.3T$.

the aneurysm. The height of the stent is observed to be more effective on vorticity reduction than the width of the stent, and the effect of width of stent on vorticity is appeared to be negligible. A similar trend was observed in $\mathrm{d}u/\mathrm{d}y$ plots in Figure 17; the red spot at the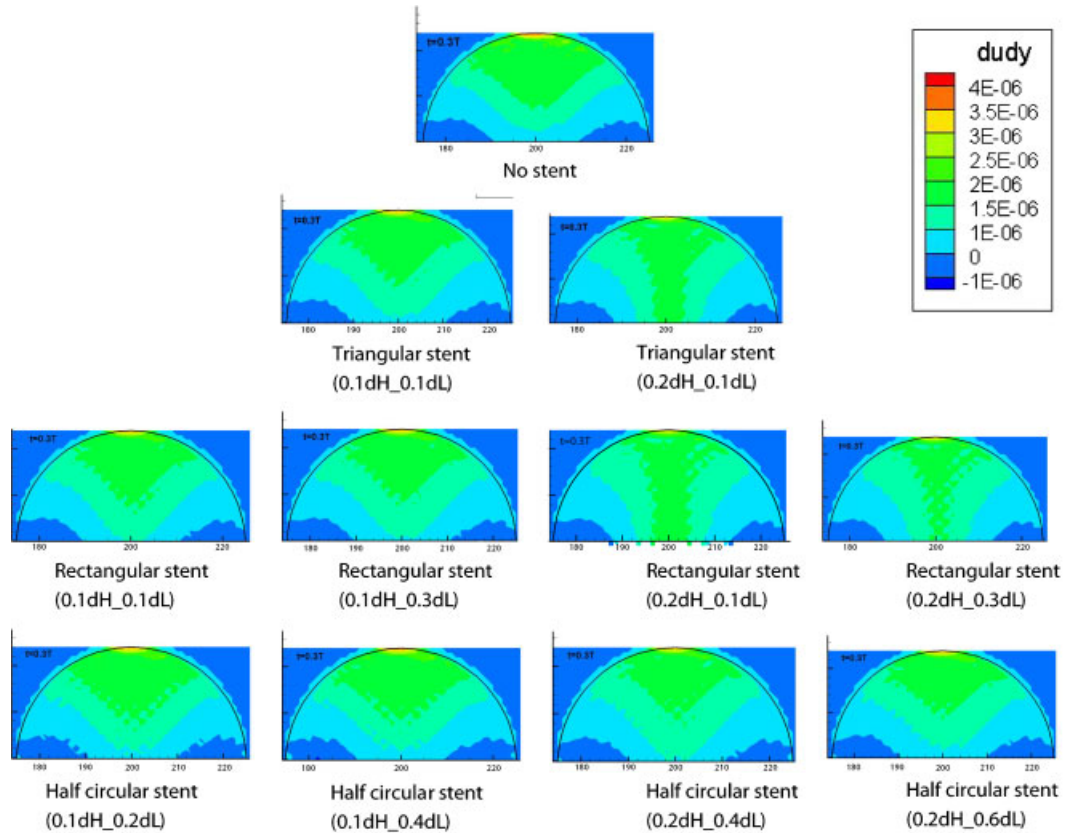 dome of the aneurysm in the non-stented case disappeared when placing a stent obstacle of any shapes. Again, the rectangular stent with $H/d=0.2$ reduced by a 21% the streamwise velocity gradient compared with the non-stented case.

The different flow patterns in an aneurysm with different stent obstacles are shown in Figure 18. The blood directly moved into the non-stented aneurysm created a large size of vortex near the dome of the aneurysm. However, the vortex is significantly reduced due to the fact that the inserted stent created a thin boundary layer over the neck of the aneurysm and kept the flow from moving into the aneurysm sac. This also led the change of vortex location to the center of the aneurysm from the vessel wall, particularly when the rectangular stent obstacle was used in the simulation.

The variation of velocities at the center of an aneurysm along the streamwise direction for stents with $H/d=0.2$ are shown in Figure 19. The reduction in velocity in the y-direction indicated less flow near the dome area of the aneurysm, which also suggested that less pressure is expected near the dome area of the aneurysm using proposed stent obstacles. When compared with the non-stented velocity in the y-direction, the maximum reduction in the peak velocity is about 15%.
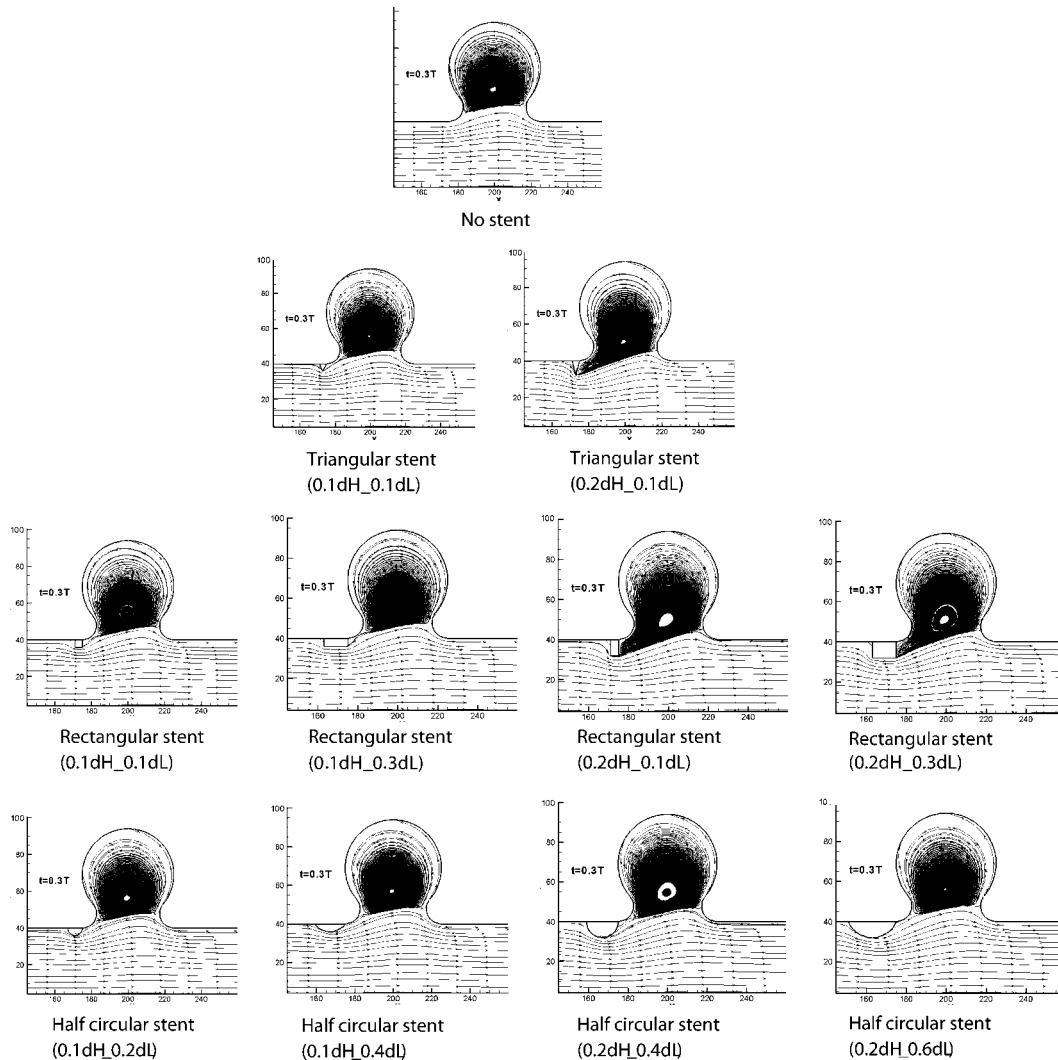
Figure 18. Comparison of velocity streamline at $t=0.3T$.

It is found that shear stress values at the dome of the aneurysm are small in all stented cases because the velocities near the dome are very small. Small shear stress values were also observed by Ohta *et al.* [41] in the dome area. Table II lists the values of shear stress, $\mu(\partial u/\partial y + \partial v/\partial x)$, and vorticity, $(\partial v/\partial x - \partial u/\partial y)$, at the top of the dome and its percentage changes compared with the non-stent obstacle case at the dome of the aneurysm. The viscosity, μ, was kept to be constant at $0.037\,\mathrm{Pa\,s}$. The rectangular stent cases reduced shear stress and vorticity most strongly as indicated in the table by the significant reduction ranging from 10.38 to 20.55%. The triangular and circular stents reduced the vorticity moderately, ranging from 6.14 to 14.3%.

The momentum of the fluid in the normal direction (ρv) and its percentage changes at the center of the aneurysm are given in Table III. As given in Table II, the rectangular stent obstacles
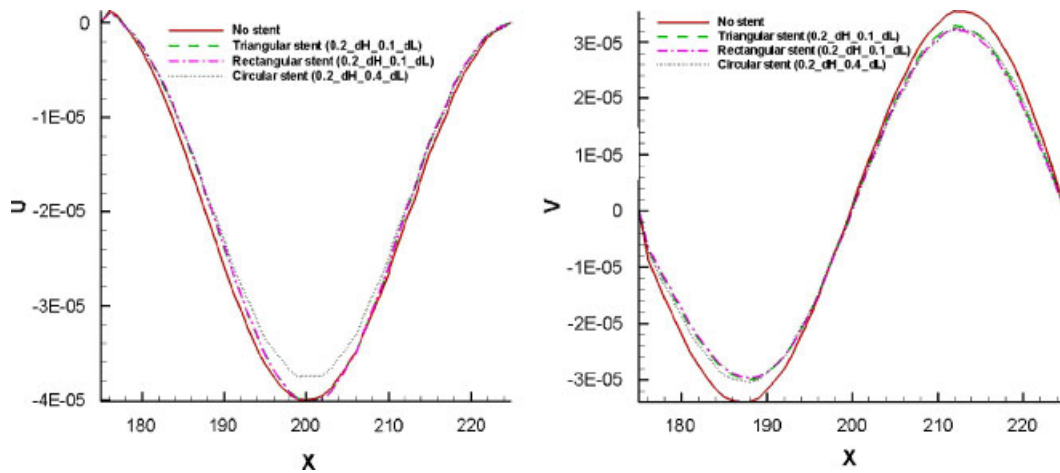
Figure 19. Velocity at the center of the aneurysm at $t = 0.3T$.

Table II. Shear stress and vorticity at the dome of the aneurysm.

Case	Shear stress (Pa)	Vorticity (1/s)	Vorticity magnitude change (%)
No stent	0.015141252	−4.0812	0.00
Triangular stent ($0.1dH\_0.1dL$)	0.013839599	−3.73035	−8.60
Rectangular stent ($0.1dH\_0.1dL$)	0.013570215	−3.65774	−10.38
Rectangular stent ($0.1dH\_0.3dL$)	0.01355864	−3.65462	−10.45
Circular stent ($0.1dH\_0.2dL$)	0.013937283	−3.75668	−7.95
Circular stent ($0.1dH\_0.4dL$)	0.014211674	−3.83064	−6.14
Triangular stent ($0.2dH\_0.1dL$)	0.012410952	−3.34527	−18.03
Rectangular stent ($0.2dH\_0.1dL$)	0.012030343	−3.24268	−20.55
Rectangular stent ($0.2dH\_0.3dL$)	0.012135336	−3.27098	−19.85
Circular stent ($0.2dH\_0.4dL$)	0.012975688	−3.49749	−14.30
Circular stent ($0.2dH\_0.6dL$)	0.013450679	−3.62552	−11.17

Table III. Momentum in the normal direction and its changes at the center of the aneurysm.

Case	ρv (kg/m^2 s)	ρv change (%)
No stent	4.16	0
Triangular stent ($0.2dH\_0.1dL$)	3.78	−8.89
Circular stent ($0.1dH\_0.2dL$)	4.13	−0.643
Circular stent ($0.1dH\_0.4dL$)	4.32	+3.96
Circular stent ($0.2dH\_0.6dL$)	4.16	−0.0753
Rectangular stent ($0.1dH\_0.1dL$)	3.05	−26.7
Rectangular stent ($0.1dH\_0.3dL$)	3.05	−26.6
Rectangular stent ($0.2dH\_0.1dL$)	2.90	−30.1

reduced the momentum moving into the aneurysm significantly. The circular stent obstacle cases are shown to be ineffective and a moderate change is observed for the triangular stent obstacle.

CONCLUSION

A two-dimensional fluid solver based on the lattice Boltzmann method (LBM) has been developed using an OOP strategy. The developed fluid solved with the LBM was compared with configurations with respect to the type of flow conditions to obtain a comprehensive comparison with analytical data. Results matched well with the analytical solutions of the channel and Couette flows.

The flow in aneurysms with simple ring-shaped stent obstacles was simulated to examine the flow inside the aneurysm. The results showed the lower vorticity near the dome of the aneurysm. Three shapes of stent (triangle, rectangle and circle) with different heights and widths have been investigated. The reduced flow, smaller vorticity magnitude and wall shear stress, and smaller du/dy near the dome of the aneurysm were observed when the proposed stent obstacles were used. The height of the stent was more effective to reduce the vorticity near the dome of the aneurysm than the width of the stent. The rectangular stent with 20% height-of-vessel radius was observed to be optimal and decreased the magnitude of vorticity by 21% near the dome of the aneurysm.

Future works for reducing the blood flow into aneurysms should include a three-dimensional implementation of the LBM, smaller artery diameters with non-Newtonian viscoelastic effect and multiphase flow with red blood cell and blood plasma. The results shown here already indicate that the current fluid solver based on the LBM is a very promising method for the blood flow analysis, particularly when complicated geometries were used. The OOP strategy can facilitate the future development of the fluid solver and ease of the coupling of particle solvers for red blood cells. More realistic artery geometry and blood models will be used in future studies.

REFERENCES

1. Geremia G, Haklic M, Brennecke L. Embolization of experimentally created aneurysms with intravascular stent devices. *American Journal of Neuroradiology* 1994; **15**:1223–1231.
2. Lieber BB, Stancampiano AP, Wakhloo AK. Alteration models by stenting: influence of stent porosity. *Annals of Biomedical Engineering* 1997; **25**:460–469.
3. Turjman F, Massoud TF, Ji C, Guglielmi G, Vinuela F, Robert J. Combined stent implantation and endosaccular coil placement for treatment of experimental wide-necked aneurysms: a feasibility study in swine. *American Journal of Neuroradiology* 1994; **15**:1087–1090.
4. Wakhloo AK, Scellhammer F, de Vries J, Haberstroh J, Schumacher M. Self-expanding and balloon-expandable stents: an experimental study in a canine model. *American Journal of Neuroradiology* 1994; **15**:493–502.
5. Wakhloo AK, Trio FO, Scellhammer F, Graf M, Hopkins LN. Self-expanding nitinol stents in canine vertebral arteries. *American Journal of Neuroradiology* 1995; **16**:1043–1051.
6. Lanzino G, Wakhloo AK, Fessler RD, Hartney ML, Guterman LR, Hopkins LN. Efficacy and current limitations of intravascular stents for intracranial internal carotid vertebral and basilar artery aneurysms. *Journal of Neurosurgery* 1999; **91**:538–546.
7. www.fda.gov/bbs/topics/news/cordis_ltr.pdf.

8. Han JC, Glicksman LR, Rohsenow WM. An investigation of heat transfer and friction for rib-roughened surfaces. *International Journal of Heat and Mass Transfer* 1978; **21**:1143–1155.

9. Bergeles G, Athanassiadis N. The flow past a surface-mounted obstacle. *Journal of Fluids Engineering* 1983; **105**:461–463.

10. Sparrow EM, Tao WQ. Enhanced heat transfer in a flat rectangular duct with streamwise-periodic disturbances at one principal wall. *Journal of Heat Transfer* 1983; **105**:851–861.

11. Drain LE, Martin S. Two-component velocity measurements of turbulent flow in a ribbed-wall flow channel. *International Conference on Laser Anenometry—Advances and Applications*, Manchester, U.K., 1985; 99–112.

12. Nourgaliev RR, Dinh TN, Sehgal BR. On lattice Boltzmann modeling of phase transition in an isothermal non-ideal fluid. *Nuclear Engineering and Design* 2002; **211**:153–171.

13. Cosgrove JA, Buick JM, Tonge SJ, Munro CG, Greated CA, Campbell DM. Application of the lattice Boltzmann method to transition in oscillatory channel flow. *Journal of Physics A* 2003; **36**:2609–2620.

14. Manz B, Gladden LF, Warren PB. Flow and dispersion in porous media: lattice-Boltzmann and NMR studies. *AIChE Journal of Fluid Mechanics and Transport Phenomena* 1999; **45**(9):1845–1854.

15. Boyd J, Buick JM, Cosgrove JA, Stansell P. Application of the lattice Boltzmann method to arterial flow simulation: investigation of boundary conditions for complex arterial geometries. *Australasian Physical and Engineering Sciences in Medicine* 2004; **27**:207–212.

16. Fang H-P, Wan R-Z, Lin Z-F. Lattice Boltzmann model with nearly constant density. *Physical Review* 2002; **66**.

17. Artoli AMM, Hoekstra AG, Sloot PMA. Mesoscopic simulations of systolic flow in the human abdominal aorta. *Journal of Biomechanics* 2006; **39**:873–884.

18. O'Connor PD, Long LN, Anderson JB. The direct simulation of detonations. *AIAA/ASME/SAE/ASEE Joint Propulsion Conference*, Sacramento, CA, July 2006. AIAA Paper No. 2006-4411.

19. Chen S, Doolen GD. Lattice Boltzmann method for fluid flows. *Annual Review of Fluid Mechanics* 1998; **30**:329–364.

20. Raabe D. Overview of the lattice-Boltzmann method for nano- and microscale fluid dynamics in materials science and engineering. *Modeling and Simulation in Materials Science and Engineering* 2004; **12**:R13–R46.

21. McNamara GR, Zanetti G. Use of the Boltzmann equation to simulate lattice gas automata. *Physical Review Letters* 1988; **61**:2332–2335.

22. Luo LS. Theory of the lattice Boltzmann method: lattice Boltzmann models for nonideal gases. *Physical Review E* 2000; **62**:4982–4996.

23. Skordos P. Initial and boundary conditions for the lattice Boltzmann method. *Physical Review E* 1993; **48**:4823–4841.

24. He H, Zou Q. Analysis and boundary condition of the lattice Boltzmann BGK model with two velocity components. *Technical Report LA-UR-95-2293*, Los Alamos National Laboratory, 1995.

25. Inamouro T, Yoshino M, Ogino F. A non-slip boundary condition for lattice Boltzmann simulations. *Physics of Fluids* 1995; **7**:2928–2930.

26. Hirabayashi M, Ohta M, Rüfenacht DA, Chopard B. A lattice Boltzmann study of blood flow in stented aneurism. *Future Generation Computer Systems* 2004; **20**:925–934.

27. Lee JS, Pletcher RH. LES of variable property turbulent flow in horizontal and vertical channels with buoyancy and heat transfer effects. *Journal of Mechanical Engineering Science* 2007; **221**(4):429–441.

28. Lee JS, Xu X, Pletcher RH. Effects of wall rotation on heat transfer to annular turbulent flow: outer wall rotating. *Journal of Heat Transfer* 2005; **127**:830–838.

29. Xu X, Lee JS, Pletcher RH. A compressible finite volume formulation for large eddy simulation of turbulent pipe flows at low Mach number in Cartesian coordinates. *Journal of Computational Physics* 2005; **203**:22–48.

30. Mittal R, Iaccarino G. Immersed boundary method. *Annual Review of Fluid Mechanics* 2005; **37**:239–261.

31. Yakhot A, Grinberg L, Nikitin N. Modeling rough stenoses by an immersed-boundary method. *Journal of Biomechanics* 2005; **38**:1115–1127.

32. Guo Z, Zheng C. An extrapolation method for boundary conditions in lattice Boltzmann method. *Physics of Fluids* 2002; **14**:2007–2010.

33. Chen S, Martinez D, Mei R. On boundary conditions in lattice Boltzmann methods. *Physics of Fluids* 1996; **8**:2527–2536.

34. Rouson D, Morris K, Xu X. Dynamic memory de-allocation in Fortran 95/2003 derived type calculus. *Scientific Programming* 2005; **13**:189–203.

35. Rouson D, Xu X, Morris K. Formal constraints on memory management for composite overloaded operations. *Scientific Programming* 2006; **14**:27–40.

36. Munson BR, Young DF, Okiishi TH. *Fundamentals of Fluid Mechanics* (5th edn). Wiley: U.S.A., 2006.
37. Guo Z, Zhen C, Shi B. Discrete lattice effects on the forcing term in the lattice Boltzmann method. *Physical Review E* 2002; **65**(4):046308.1–046308.6.
38. Won JY, Suh S, Ko H, Lee KH, Shim WH, Chang B, Choi DH, Park SJ, Lee DY. Problems encountered during and after stent–graft treatment of aortic dissection. *Journal of Vascular and Interventional Radiology* 2006; **17**:271–281.
39. Lieber BB, Stancampiano AP, Wakhloo AK. Alteration of hemodynamics in aneurism models by stenting: influence on stent porosity. *Annals of Biomedical Engineering* 1997; **25**(3):460–469.
40. Sahjpaul RL, Abdulhak MM, Drake CG, Hammond RR. Fatal traumatic vertebral artery aneurysm rupture, case report. *Journal of Neurosurgery* 1998; **89**:822–824.
41. Ohta M, Wetzel SG, Dantan P, Bachelet C, Lovblad KO, Yilmaz H, Flaud P, Rufenacht DA. Rheological changes after stenting of a cerebral aneurysm: a finite element modeling approach. *Cardiovascular and Interventional Radiology* 2005; **28**:768–772.